



Development of an Aerodynamic Analysis Methodology for Segmented Ultralight Morphing Rotors

Suraj Bansal,^{*} Gavin K. Ananda,[†] and Michael S. Selig[‡]
University of Illinois at Urbana-Champaign, Urbana, IL 61801, USA

The Segmented Ultralight Morphing Rotor (SUMR) concept for a 50 MW wind turbine will help alleviate the technical challenges presented by a conventional upwind rotor design for such extreme-scale wind turbines. Such segmented rotor blades can be morphed to achieve load alignment which will significantly reduce the cantilever moments, thus allowing for a lighter blade design. Depending on the wind speed, these rotors may be morphed into highly coned configurations. Consequently, a computational tool was developed in this study for the analysis of the SUMR rotors in different morphing configurations. The analysis tool was developed by modifying the Blade Element Momentum method for the morphing rotor geometry. The model was implemented in a MATLAB code, BladeMorph, and will be subsequently combined with PROPID for the purpose of rapid design and analysis of the large-scale SUMR rotors. An example 13 MW SUMR rotor, referred to as the E-13 rotor in this paper, was designed in PROPID and analyzed in BladeMorph for various cone angles to obtain the C_p and C_T vs tip speed ratio curves and radial distributions of pertinent aerodynamic parameters. The predictions from BladeMorph were then compared with AeroDyn v14, and it was found that the predictions from both codes were in fairly good agreement. A large reduction in both rotor power and rotor thrust coefficients with an increase in coning angles was found. The angles of attack α , lift coefficient C_l , and drag coefficient C_d along the blade length were reduced at higher coning, while the variation in the net relative velocity, Reynolds number, and dynamic pressure along the blade was found to be minimal. Finally, with increasing coning, the axial induction distribution was found to increase toward the outboard region of the blade compared with the zero coning case, while decreasing near the inboard region of the blade.

Nomenclature

a	= axial induction factor
a'	= circumferential (tangential) induction factor
$A_{S_{n,proj}}$	= projected area of each blade station
A_{S_n}	= area of each blade station
AR	= blade aspect ratio
B	= number of blades
C_d	= 2D drag coefficient
C_l	= 2D lift coefficient
C_P	= rotor power coefficient, $\frac{P}{\frac{1}{2}\rho V_0^3 S_d}$
C_Q	= rotor torque coefficient, $\frac{Q}{\frac{1}{2}\rho V_0^2 S_d R_T}$
c_{S_n}	= chord at any blade station
$C_{T_{Local}}$	= head loss coefficient (local thrust coefficient)
C_T	= rotor thrust coefficient, $\frac{P}{\frac{1}{2}\rho V_0^2 S_d}$
D	= drag force
F	= combined tip loss correction, $F = F_H F_T$
F_H	= hub loss correction
f_H	= Prandtl hub loss correction exponent
F_T	= tip loss correction
f_T	= Prandtl tip loss correction exponent
L	= lift force
l_i	= length of each segment blade, where $i = 1, 2, \dots, N$
N	= number of blade segments

^{*}Graduate Research Assistant, Department of Aerospace Engineering, AIAA Student Member. sbansal5@illinois.edu

[†]Graduate Research Assistant (Ph.D. Candidate), Department of Aerospace Engineering, AIAA Student Member. anandak1@illinois.edu

[‡]Professor, Department of Aerospace Engineering, AIAA Associate Fellow. m-selig@illinois.edu

n	= number of blade stations
P	= power
Q	= torque
R_H	= rotor hub radius
R_T	= blade tip radius
R_{S_n}	= radius of each discretized blade station
$R_{S_{n,proj}}$	= projected radius of each discretized blade station
$R_{T_{proj}}$	= projected blade tip radius
Re	= Reynolds number, $\frac{Wc}{\nu}$
S_d	= rotor swept area
$S_{d_{proj}}$	= projected rotor swept area
$S_{d_{S_n}}$	= annular swept area
$S_{d_{S_{n,proj}}}$	= projected annular swept area
T	= thrust
V_0	= wind speed
V_{as_n}	= axial wind speed at the rotor plane
V_{ns_n}	= component of axial flow normal to the blade
$V_{T_{S_n}}$	= tangential speed of the blade station
W	= net relative velocity seen by each discretized blade station
X	= tip speed ratio, $X = \omega R_{T_{proj}} / V_0$
α	= angle of attack
β	= total twist
β_r	= relative blade twist
ΔR_{S_n}	= length of each discretized blade station
$\Delta R_{S_{n,proj}}$	= projected length of each discretized blade station
$\Delta\beta$	= blade pitch
ν	= flow kinematic viscosity
ω	= blade rotational speed
ϕ	= inflow angle
ψ	= coning angle
ρ	= flow density
σ'_{S_n}	= local solidity

I. Introduction

To meet the aim envisioned by the US Department of Energy, which is to produce 20 percent of electricity by the year 2030 using wind energy,¹ ARPA-E recently awarded a contract to a group of institutions to design a low-cost offshore 50 MW wind turbine in order to help accelerate the development of the US offshore wind energy capability.² Such an extreme-scale wind turbine will produce a great amount of technical barriers, if designed using conventional methods. Some of the technical and economical difficulties when designed using conventional method will involve a) rapidly increasing blade mass at such extreme-scales (about 200 m blade length for 50 MW) due to high blade stiffness in order to avoid the possibility of tower strikes, b) blade manufacturing and transportation difficulties largely due its large radius, and c) prohibitive costs.^{3,4} Hence, a different approach must be adopted in order to design such extreme-scale wind turbine rotors.

A group of institutions led by the University of Virginia (UVA), including the University of Colorado-Boulder (UCB), Colorado School of Mines (CSM), National Renewable Energy Laboratory (NREL), Sandia National Laboratories (SNL), and University of Illinois at Urbana-Champaign (UIUC), have proposed the Segmented Ultralight Morphing Rotor (SUMR) concept to overcome these extreme-scale technical barriers.⁵ The SUMR concept uses a downwind rotor with segmented blades, where each segment can be coned at a different angle to align the net force resulting from the gravitational, centrifugal, and the aerodynamic forces along the blades such that the downwind cantilever loads are reduced dramatically (see Fig. 1).³ Morphing the rotor blades to such load-aligned configurations will lead to a drastic reduction in the blade mass, thus allowing for an ultralight blade design. Various states of morphing for the proposed rotor concept are shown in Fig. 2. At low wind speeds, the rotor will have zero coning to maximize

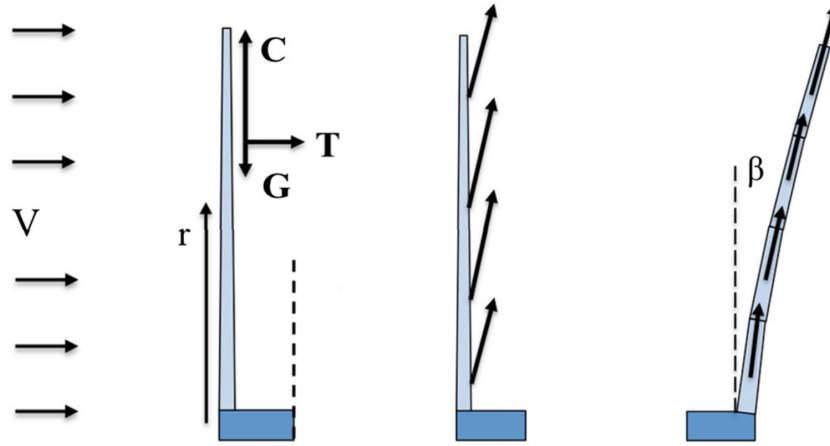


Figure 1. Diagram depicting load alignment for a morphing downwind rotor at rated conditions to reduce cantilever moments. Taken from Steele et al.³

the amount of wind energy captured, while at the rated speeds the rotor will be morphed in the load aligned state. To withstand extreme hurricane wind speeds at offshore locations, the rotor may be morphed into a stowed configuration. From Fig. 2, it becomes clear that the rotor blades may be highly coned, especially as the wind approaches higher speed. Hence, the SUMR concept requires the use of an aerodynamic analysis methodology capable of analyzing highly coned rotors.

Most computational aerodynamic analysis tools for wind turbine rotors at their very core employ the use of Blade Element Momentum Theory (BEMT), largely due to the ease of implementation and reduced computational time. Over the years, as the wind turbines have evolved progressively larger, greater blade deflections due to aeroelastic effects have prompted researchers to develop different modifications to the BEM models for studying the effects of coning. Mikkelsen et al.⁷ investigated the effect of coning a wind turbine rotor using two different approaches including a) BEM and b) an actuator disk method coupled with the Navier-Stokes equations. The 2 MW Tjaereborg wind turbine was analyzed, and it was found that even though the power was reduced at 20 deg coning, the C_P obtained by nondimensionalizing power using the projected rotor area did not change much ($\approx 1\%$). Also, considerable changes in the radial distribution of interference factors was found when coned at 20 deg, compared with the corresponding radial distributions at zero coning, which was explained by the change in position of the rotor with respect to the trailing vortex system.

Madsen et al.⁸ compared the BEM predictions with CFD results for a coned actuator disk in order to validate the BEM method and to find the validity of the assumptions behind the equations that model the flow through the rotor. Upon comparison of the two methods, it was found that for a disk loading corresponding to maximum C_P , the overall rotor C_P predictions from both methods were close, but the radial distribution of the local C_P from both methods did not agree well. In the inboard region, the local C_P predicted using BEM was lower while toward the outboard region, the local C_P predictions from BEM were higher compared with the CFD analysis of the coned actuator disk. Such discrepancies occurred as a result of the failure to account for the pressure variation from wake rotation in the inboard regions and decreased inflow near the tip region due to wake expansion, in the BEM approach. Subsequently, two models to account for the pressure variation in the rotating wake and the decreased inflow due to wake expansion were implemented in their BEM code, which improved the agreement between BEM and CFD predictions for the actuator disk.

Crawford⁹ reviewed the validity of underlying assumptions behind the BEM method for suitable modification of the method to model highly coned rotors. The effects of the inflow turbulence, yaw, and wind shear were all neglected, and the analysis was assumed to be steady and axisymmetric. The radial component of the inflow velocity at the rotor plane was considered in the analysis for greater accuracy, which in the conventional BEM approach is usually assumed to be zero. The induction factors at the rotor plane were obtained through a complex wake analysis method, modeled based on the potential flow theory and the Biot-Savart law. Using their modified BEM model, the results were presented and compared with CFD studies for validation. The author⁹ concluded that the main reason for errors

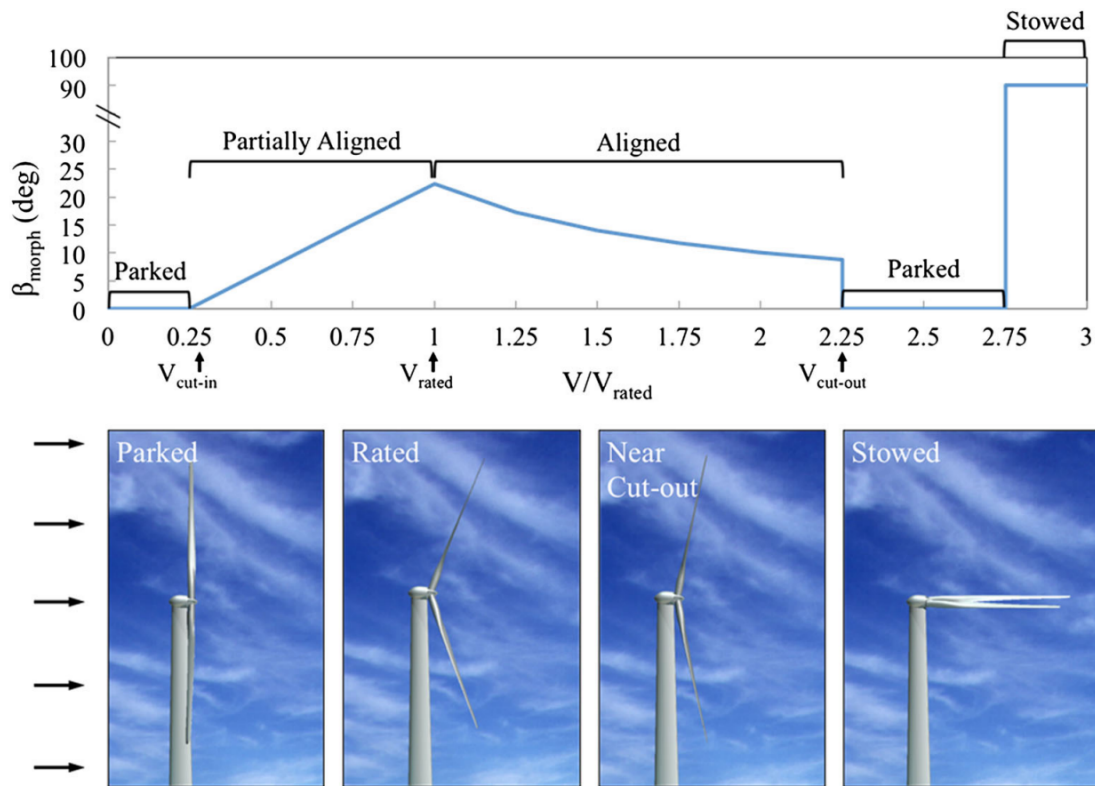


Figure 2. Conceptual representation of different rotor morphing configurations based on the wind speed: a) parked configuration, b) rated configuration, c) near cut-out configuration, and d) stowed configuration. Taken from Ichter et al.⁶

in the BEM method was the Bernoulli-derived relation between the freestream and farfield velocity, which becomes inaccurate when the radial component of the flow is included in the analysis. The importance of choosing an accurate thrust model for large values of the axial induction factors was also highlighted. Crawford and Platts¹⁰ performed a design optimization study for coned rotors with a flapping hinge using their modified BEM model and presented results for C_P vs tip speed ratio for different coning angles ranging from 0 to 50 deg, where the C_P was found to be decreasing significantly with increasing coning angles.

Hibbs and Radkey¹¹ investigated the flowfield around a highly coned rotor while considering rotor shaft tilt and wind shear effects and implemented their model in a FORTRAN code named PROP.¹² However, the PROP code does not have the capability of analyzing rotor blades with segmented multiconing. Given the possible use of segmented multiconing for the 50 MW rotor design, it became necessary to develop a new method for the analysis of SUMR rotors with segmented multiconing. Hence, this study builds upon the work of Hibbs and Radkey¹¹ and modifies their approach to include the analysis capability for segmented wind turbine rotors with a radially varying coning angle distribution. The model derived in this study has the ability of analyzing the SUMR rotor in various morphing configurations and has been implemented in a MATLAB code, BladeMorph. BladeMorph has the additional capabilities such as nonuniform discretization of the blades to account for the location of the morphing hinges and calculation of power and aerodynamic loads based on a morphing and pitch schedule, where the coning angles and the pitch of the blade can vary with wind speeds. Although Blademorph has been used as a standalone code for the purpose of this study, it will be subsequently combined with PROPID^{13,14} (via a graphical user interface) to facilitate the rapid design and analysis of the SUMR rotor.

II. Description of the Analytical Model

In this section, a set of BEM equations based on the analytical model presented by Hibbs and Radkey¹¹ has been derived in order to analyze the aerodynamic performance of downwind SUMR rotors. The BEM method uses the traditional strip theory approach which has proven to be quite effective in the analysis of propellers and conventional wind turbines. Using the strip theory approach, the rotor blades have been broken down into a number of discretized elements, henceforth referred to as blade stations in this paper. Of course, while taking advantage of the strip theory approach, it is tacitly assumed that the adjacent blade stations do not interact with each other, thus implying zero radial flow on the rotor blades. Another inherent assumption made by the BEM theory is that the forces acting on these blade stations are purely aerodynamic in nature and that these aerodynamic forces are the only ones that affect the flow.

The SUMR rotor can primarily have three types of geometric configurations: a) zero coning, b) single coning, and c) segmented multiconing. As the name suggests, the zero coning case is a non-morphed geometric configuration which occurs when the coning angle ψ is zero in Fig. 3a. Similarly, the single coning morphing configuration occurs when $\psi \neq 0$, i.e., when the straight rotor blades are morphed near the hub at a certain non-zero coning angle relative to the rotor plane. Finally, the segmented multiconing mode of morphing the rotor can be defined as the geometric configuration in which different segments of the rotor blades achieve different coning angles relative to the rotor plane, as shown in Fig. 3b. Since the segmented multiconing method of morphing is the most general case (single coning morphing method is the subset of this case), all mathematical equations have been derived for the segmented multiconing method of morphing the rotor geometry.

Figure 3a shows a two-bladed downwind rotor with single coning. The tip radius of the rotor when the coning angle ψ is set to zero is R_T . In the case of a segmented rotor blade (Fig. 3b), the unconed rotor tip radius R_T is the sum of the lengths of individual blade segments l_i and the hub radius R_H , given by

$$R_T = R_H + l_1 + l_2 + l_3 + \dots + l_N \quad (1)$$

where, l_1, l_2, \dots, l_N are the lengths of the N segments on the SUMR blade. The number of segments will typically vary from three to five for the SUMR rotors, depending on its size. A SUMR rotor blade with three segments has been shown in Fig. 4b.

The radius of the swept area projected on the rotor plane by the rotor in the segmented multiconing morphed state can be calculated using

$$R_{T_{proj}} = R_H + l_1 \cos \psi_1 + l_2 \cos \psi_2 + l_3 \cos \psi_3 + \dots + l_N \cos \psi_N \quad (2)$$

Since this analysis uses the strip theory approach, the unmorphed blades will be discretized into various radial blade stations each having a length ΔR_{S_n} , where the n^{th} radial blade station is denoted as S_n .

When the blades are morphed to have segmented multiconing, the projected length of the S_n radial blade station becomes

$$\Delta R_{S_{n,proj}} = \Delta R_{S_n} \cos \psi_{S_n} \quad (3)$$

The projected radius of each blade station can be computed using

$$R_{S_{n,proj}} = \sum_{k=1}^{n-1} \Delta R_{S_{k,proj}} + \frac{\Delta R_{S_{n,proj}}}{2} \quad (4)$$

where the projected radius of each blade station is measured from the rotor axis to the center of the projected blade station on the rotor plane. It is at the center of these projected blade stations where each of the quantities of interest are computed. Typically, in the case of zero or single coning, the blades will be discretized with blade elements of equal size (as shown in Fig. 4a), while in the segmented multiconing case the blades will be most likely discretized nonuniformly, based on the hinge locations (as shown in Fig. 4b). The nonuniform method of blade discretization will in general result in a higher number of blade elements when compared with the uniform blade discretization.

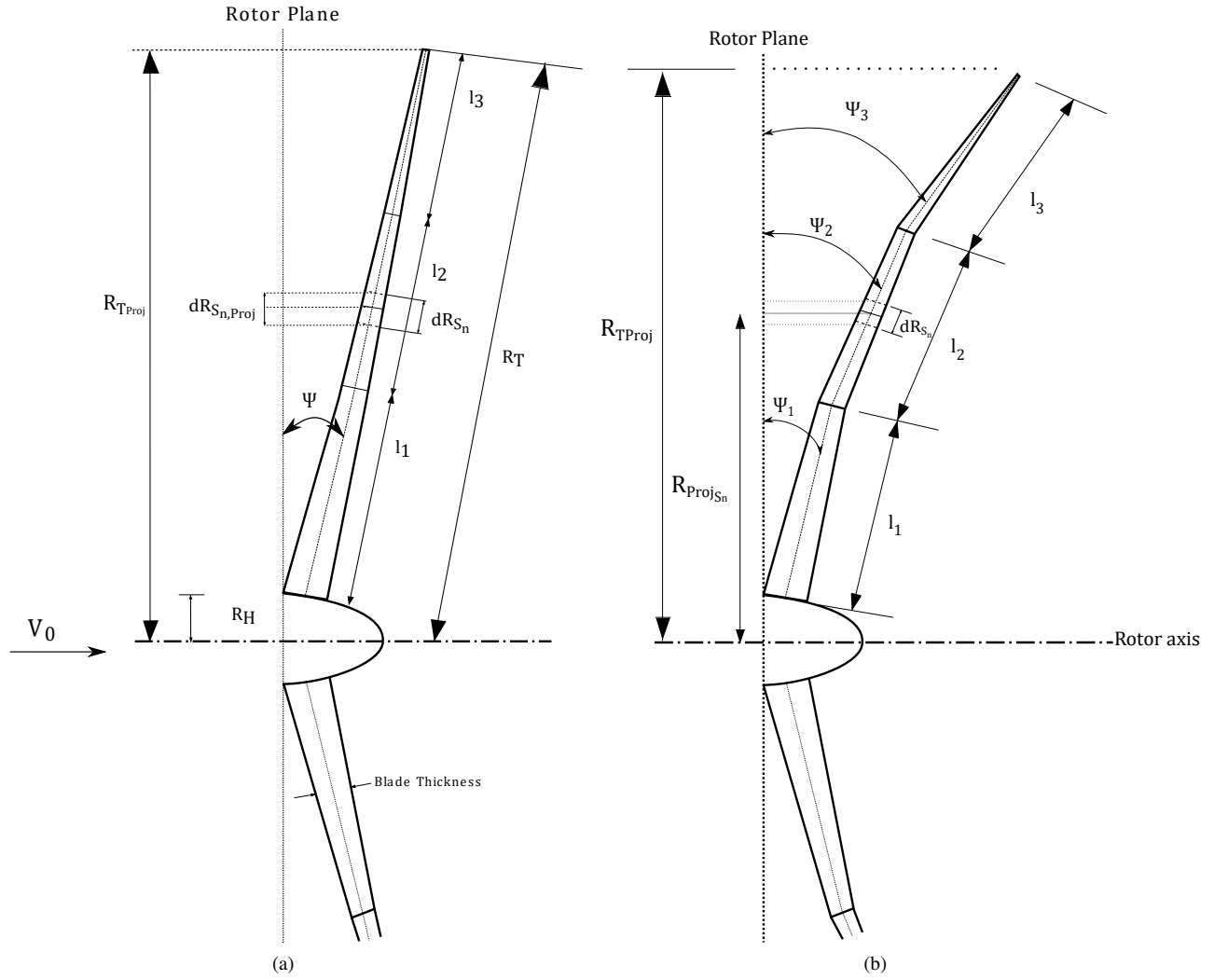


Figure 3. Diagram depicting two primary modes of morphing the rotor blades: (a) single coning and (b) segmented multiconging.

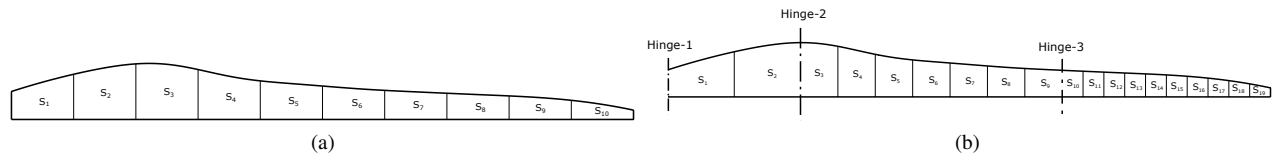


Figure 4. Blade discretization method based on two modes of coning the rotor: a) zero coning and single coning and b) segmented multiconging.

The radius of the projected area can also be calculated as

$$R_{T_{proj}} = \Delta R_{S_{1,proj}} + \Delta R_{S_{2,proj}} + \dots + \Delta R_{S_{n,proj}} \quad (5)$$

The projected area is then given by

$$S_{d_{proj}} = \pi R_{T_{proj}}^2 \quad (6)$$

Hibbs and Radkey¹¹ used the projected rotor area calculated using Eq. 6 to nondimensionalize quantities such as the rotor power P , thrust T , and torque Q . However, it becomes much easier for the purpose of analysis and comparison to have physical quantities nondimensionalized by fixed reference quantities. Hence, the nondimensional quantities will be calculated using the unmorphed rotor area given by

$$S_d = \pi R_T^2 \quad (7)$$

The area of each discretized blade station can be estimated using

$$A_{S_n} = c_{S_n} \Delta R_{S_n} \quad (8)$$

It is to be noted that while calculating the area of each blade station, the effect of radially varying chord distribution is not taken into account, i.e., the chord is assumed constant for the entire blade station, thus approximating the shape of the blade station to be rectangular. The area projected by the blade station on the rotor plane can be calculated using

$$A_{S_{n,proj}} = c_{S_n} \Delta R_{S_{n,proj}} \quad (9)$$

In Eq. 9, the effect of reduction in the projected area due to the blade twist is not taken into account, i.e., the projected chord length is assumed to be the same as the actual length of the chord at that radial location. The projected area of the annulus swept by a given blade station when the rotor is spinning can be calculated from

$$\Delta S_{d_{S_{n,proj}}} = 2\pi R_{S_{n,proj}} \Delta R_{S_{n,proj}} \quad (10)$$

The local solidity is defined as

$$\sigma'_{S_n} = \frac{B c_{S_n}}{\pi R_{S_{n,proj}}} \quad (11)$$

From Eq. 11, it is evident that the solidity of the rotor increases when the rotor is morphed at a certain coning angle. The tip speed ratio is defined as the ratio of the tangential velocity of the rotor tip (tip speed) to the freestream wind velocity and is given by

$$X = \frac{\omega R_{T_{proj}}}{V_0} \quad (12)$$

It is worth noting that Eq. 12 has the term $R_{T_{proj}}$ instead of the tip radius R_T . Since variable speed wind turbines operate at a constant tip speed ratio, the rotor will have to spin faster (higher ω) when coned at a certain angle in order to maintain the tip speed ratio.

Figure 5 illustrates the flow streamlines as they pass through the rotor. The flow far upstream is approaching the rotor at a freestream wind velocity V_0 and is assumed to flow parallel to the rotor axis, i.e., the freestream flow is perpendicular to the rotor plane and has a zero yaw angle. Uniform inflow (no wind shear) and zero rotor tilt is assumed throughout this study. Since the kinetic energy of the wind is extracted in order to spin the wind turbine rotor, the incoming freestream flow experiences a speed reduction as it approaches the rotor which is manifested by the gradually expanding streamlines. Thus, the axial flow velocity that the rotor blade station experiences becomes

$$V_{a_{S_n}} = V_0 (1 - a_{S_n}) \quad (13)$$

where, a_{S_n} is the axial induction factor and represents the amount by which the incoming freestream flow has decelerated at the rotor plane. It should be noted that the expansion of flow streamlines around the rotor indicates the presence

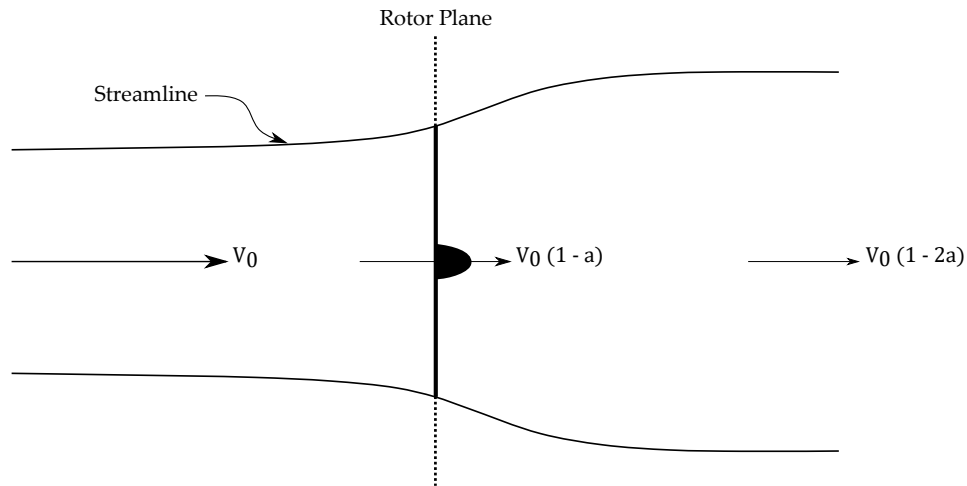


Figure 5. Diagram depicting the expanding streamlines as the incoming freestream flow passes through the rotor.

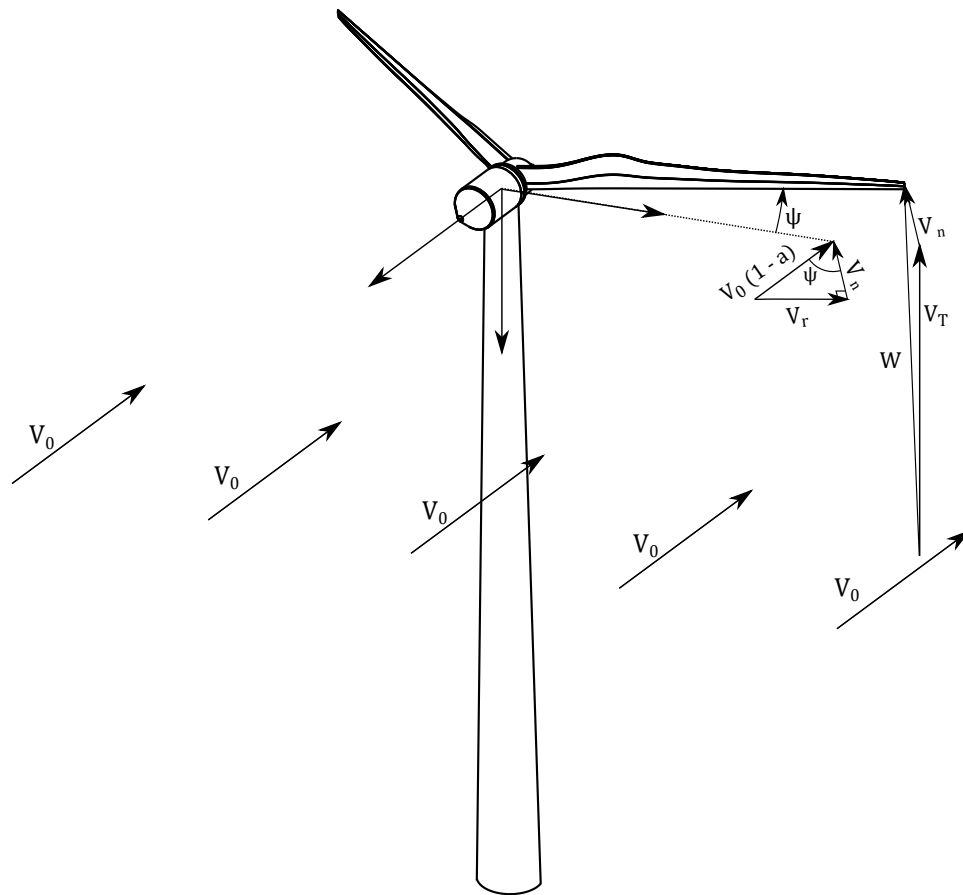


Figure 6. Diagram illustrating a wind turbine rotor with single coning and the flowfield as seen by the rotor blades.

of a radial component of the flow. Nevertheless, the radial component of the flow is assumed to be zero, similar to traditional BEM models for the purpose of simplicity.

The manner in which morphing the rotor affects the surrounding flowfield can be seen in Fig. 6. When the blades

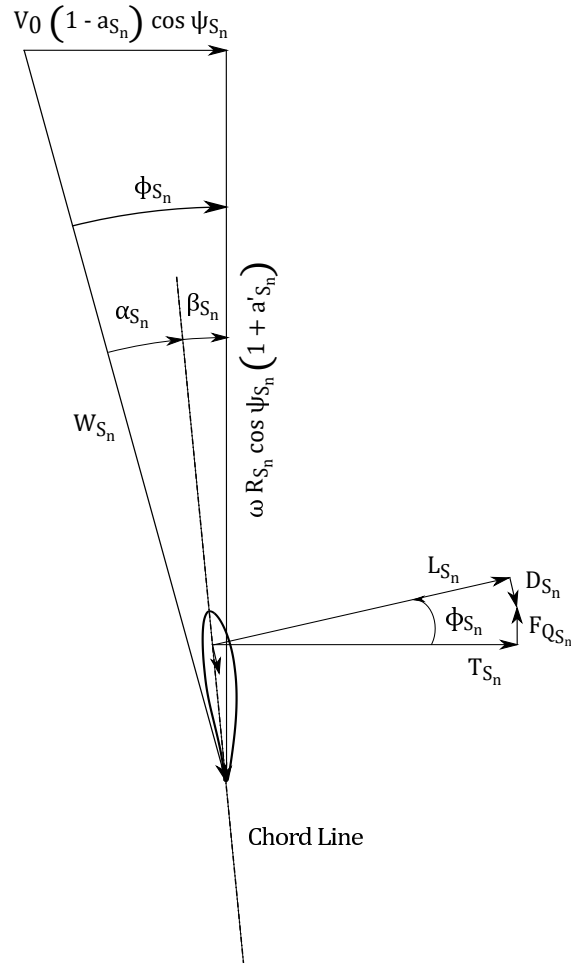


Figure 7. Velocity and force diagrams for a given radial blade station

are coned at a given angle, the component of axial flow normal to the blade becomes

$$V_{n_{S_n}} = V_{a_{S_n}} \cos \psi_{S_n} = V_0 (1 - a_{S_n}) \cos \psi_{S_n} \quad (14)$$

Figure 7 represents the velocity and force vectors acting on a given blade station. The tangential velocity of the blade station when the rotor is spinning with an angular velocity ω is given by

$$V_{T_{S_n}} = \omega R_{S_n,proj} (1 + a'_{S_n}) \quad (15)$$

where a'_{S_n} is the tangential induction factor. The net relative velocity actually seen by the blade station is then calculated using

$$W_{S_n} = \sqrt{V_{n_{S_n}}^2 + V_{T_{S_n}}^2} \quad (16)$$

or

$$W_{S_n} = V_0 \sqrt{(1 - a_{S_n})^2 \cos^2 \psi_{S_n} + X^2 \left(\frac{R_{S_n,proj}}{R_{T,proj}} \right)^2 (1 + a'_{S_n})^2} \quad (17)$$

The inflow angle ϕ made by the net relative flow velocity W and the rotor plane is estimated using the following

$$\phi_{S_n} = \tan^{-1} \left[\left(\frac{R_{T,proj}}{R_{S_n,proj}} \right) \frac{(1 - a_{S_n}) \cos \psi_{S_n}}{X(1 + a'_{S_n})} \right] \quad (18)$$

The angle of attack α is calculated as

$$\alpha_{S_n} = \phi_{S_n} - \beta_{S_n} \quad (19)$$

where β_{S_n} is the sum of the relative blade twist (β_r) and the blade pitch angle ($\Delta\beta$).

The Reynolds number at a given blade station can be determined using

$$Re_{S_n} = \frac{c_{S_n} W_{S_n}}{\nu} \quad (20)$$

The lift and drag coefficients can be obtained from the provided airfoil data using the angle of attack and the Reynolds number calculated above

. Since the number of blade stations on the blade span can be, say, 10 or more, the airfoil data for airfoils at each of the blade stations are not provided for the sake of simplicity and convenience. Instead, airfoils at specific locations are specified and their data are provided. The airfoil data at these specified locations consist of tabulated values of C_l and C_d over a range of angles of attack and Reynolds number. The airfoil data for the intermediate blade stations are obtained using linear interpolation between these specified airfoils.

The lift and drag forces acting on the blade stations can be resolved into axial and tangential components. The axial component of the resultant aerodynamic force is called the thrust force, while the tangential component of the resultant force vector creates the torque to spin the rotor. From Eq. 7, the thrust component for a single blade station can be written as

$$\Delta T_{S_n} = (L_{S_n} \cos \phi_{S_n} + D_{S_n} \sin \phi_{S_n}) \cos \psi_{S_n} \quad (21)$$

Similarly, the tangential component of the resultant aerodynamic force can be written as

$$\Delta F_{Q_{S_n}} = L_{S_n} \sin \phi_{S_n} - D_{S_n} \cos \phi_{S_n} \quad (22)$$

Since the inflow angle values are usually not large at the design conditions (less than 30 deg) and have even lower values toward the blade tip, it is interesting to see that the component of the lift force that aids in spinning the rotor ($L \sin \psi$) is actually a lot smaller than the component of the lift force that acts in the thrust direction ($L \cos \psi$). From Eq. 22, it becomes apparent that even though this equation does not have an explicit coning angle term, the value of $\Delta F_{Q_{S_n}}$ will be still be affected by changing the coning angle. This is due to the fact that the inflow angle ϕ , lift L , and drag force D are cone angle dependent.

The resulting torque generated by any blade station can be computed as below

$$\Delta Q_{S_n} = \Delta F_{Q_{S_n}} R_{S_n,proj} \quad (23)$$

Now that the velocity and force components have been resolved suitably, the axial and tangential induction factors can be computed by equating the forces on the blade stations with the change in flow momentum across those blade stations. Equation 21 estimates the thrust force generated on a single blade station. The thrust force on all the blade elements in a given annulus can be computed by adding their individual contributions, viz.

$$\Delta T_{S_n} = B(L_{S_n} \cos \phi_{S_n} + D_{S_n} \sin \phi_{S_n}) \cos \psi_{S_n}$$

Or

$$\Delta T_{S_n} = \frac{1}{2} B \rho W_{S_n}^2 (c_{S_n} \Delta R_{S_n}) [C_{l_{S_n}} \cos \phi_{S_n} + C_{d_{S_n}} \sin \phi_{S_n}] \cos \psi_{S_n} \quad (24)$$

The pressure drop across a given annulus, calculated using the momentum theory¹⁵, is given as

$$\Delta P_{S_n} = \frac{1}{2} \rho V_0^2 C_{T_{LocalS_n}} \quad (25)$$

where $C_{T_{localS_n}}$ is the local thrust coefficient, also known as the head loss coefficient, and is given by

$$C_{T_{LocalS_n}} = 4a_{S_n} (1 - a_{S_n}) \quad (26)$$

Hence, the thrust force from the resulting pressure drop can be calculated as below

$$\Delta T_{S_n} = \Delta P_{S_n} S_{d_{S_n,proj}} = \frac{1}{2} \rho V_0^2 4a_{S_n} (1 - a_{S_n}) (2\pi R_{S_n,proj} \Delta R_{S_n,proj}) \quad (27)$$

It is important to note that the local thrust coefficient or the head loss coefficient is derived by nondimensionalizing the annular thrust force with the projected annulus area and not the actual annulus area.

The BEMT equations fail to account for the effects of tip vortices and reduced loading near the tips as a result of which, they end up overpredicting the torque and hence, the power generated from the rotor. The Prandtl tip loss model¹¹ suitably accounts for the effects of tip vortices and is described as below

$$F_{T_{S_n}} = \frac{2}{\pi} \cos^{-1} (e^{-f_{T_{S_n}}}) \quad (28)$$

$$f_{T_{S_n}} = \frac{B}{2} \left(\frac{R_T - R_{S_n}}{R_T \sin \phi_T} \right) \approx \frac{B}{2} \left(\frac{R_T - R_{S_n}}{R_{S_n} \sin \phi_{S_n}} \right) \quad (29)$$

$$F_{H_{S_n}} = \frac{2}{\pi} \cos^{-1} (e^{-f_{H_{S_n}}}) \quad (30)$$

$$f_{H_{S_n}} = \frac{B}{2} \left(\frac{R_{S_n} - R_H}{R_H \sin \phi_{S_n}} \right) \quad (31)$$

$$F_{S_n} = F_{T_{S_n}} F_{H_{S_n}} \quad (32)$$

When the tip loss model is turned off, tip loss factor is then

$$F_{S_n} = 1 \quad (33)$$

The tip loss factors are included in the momentum equations by using the terms $F_{S_n} a_{S_n}$ and $F_{S_n} a'_{S_n}$ instead of a_{S_n} and a'_{S_n} , respectively.¹¹ Using the tip loss model above and by equating Eq. 24 and Eq. 27 yields

$$\frac{1}{2} \rho V_0^2 4 F_{S_n} a_{S_n} (1 - F_{S_n} a_{S_n}) (2\pi R_{S_n,proj} \Delta R_{S_n,proj}) = \frac{1}{2} B \rho W_{S_n}^2 (c_{S_n} \Delta R_{S_n}) [C_{l_{S_n}} \cos \phi_{S_n} + C_{d_{S_n}} \sin \phi_{S_n}] \cos \psi_{S_n} \quad (34)$$

Ignoring the contribution of drag term gives

$$4 F_{S_n} a_{S_n} (1 - F_{S_n} a_{S_n}) = \frac{\sigma'_{S_n} \cos^2 \psi_{S_n}}{2 \sin^2 \phi_{S_n}} (1 - a_{S_n})^2 C_{l_{S_n}} \cos \phi_{S_n} \quad (35)$$

Using the approach of the classical brake state model,¹¹ a new variable $S_{w_{S_n}}$ can be defined viz.

$$S_{w_{S_n}} = \left(\frac{\sigma'_{S_n}}{8} \right) \frac{C_{l_{S_n}} \cos \phi_{S_n} \cos^2 \psi_{S_n}}{\sin^2 \phi_{S_n}} \quad (36)$$

Using Eq. 35–36, an expression for the axial induction factor can be obtained as follows

$$a_{S_n} = \frac{2 S_{w_{S_n}} + F_{S_n} - \sqrt{F_{S_n}^2 + 4 S_{w_{S_n}} F_{S_n} (1 - F_{S_n})}}{\frac{1}{2} (S_{w_{S_n}} + F_{S_n}^2)} \quad (37)$$

Now, from Eq. 21, the torque generated on the blade elements in a given annulus can also be written as

$$\Delta Q_{S_n} = \frac{1}{2} B \rho W_{S_n}^2 (c_{S_n} \Delta R_{S_n}) [C_{l_{S_n}} \sin \phi_{S_n} - C_{d_{S_n}} \cos \phi_{S_n}] R_{S_n,proj} \quad (38)$$

Assuming no wake expansion, and from the fact that circumferential velocity in the wake is twice the circumferential velocity at the rotor,^{7,11,15,16} the rate of change of the angular momentum of the flow across the annular streamtube can be expressed as follows

$$\Delta Q_{S_n} = m_{S_n} (2\omega R_{S_n,proj} a'_{S_n}) R_{S_n,proj} \quad (39)$$

The mass flowrate m_{S_n} through the annular streamtube and is calculated as below

$$m_{S_n} = \rho V_0 (1 - a_{S_n}) (2\pi R_{proj_{S_n}} \Delta R_{S_n,proj}) \quad (40)$$

From Eqs. 39 and 40, the rate of change of angular momentum of the flow can be rewritten as

$$\Delta Q_{S_n} = 4\pi \rho V_0 (R_{S_n,proj}^3 \Delta R_{S_n,proj}) \omega a'_{S_n} (1 - a_{S_n}) \quad (41)$$

Equating Eq. 38 and 41 gives

$$4\pi\rho V_0 \left(R_{S_{n,proj}}^3 \Delta R_{S_{n,proj}} \right) \omega a'_{S_n} (1 - a_{S_n}) = \frac{1}{2} B \rho W_{S_n}^2 (c_{S_n} \Delta R_{S_n}) \left[C_{l_{S_n}} \sin \phi_{S_n} - C_{d_{S_n}} \cos \phi_{S_n} \right] R_{S_{n,proj}} \quad (42)$$

which simplifies to

$$\frac{a'_{S_n}}{1 + a'_{S_n}} = \left(\frac{\sigma'_{S_n}}{8} \right) \frac{\left[C_{l_{S_n}} \sin \phi_{S_n} - C_{d_{S_n}} \cos \phi_{S_n} \right]}{\sin \phi \cos \phi} \quad (43)$$

Ignoring the contribution of the drag term¹¹ gives

$$\frac{a'_{S_n}}{1 + a'_{S_n}} = \left(\frac{\sigma'_{S_n}}{8} \right) \frac{C_{l_{S_n}}}{\cos \phi} \quad (44)$$

Let C_1 be defined the following way (including the tip loss effects)

$$C_1 = \left(\frac{\sigma'_{S_n}}{8F_{S_n}} \right) \frac{C_{l_{S_n}}}{\cos \phi} \quad (45)$$

then

$$a'_{S_n} = \frac{C_1}{1 - C_1} \quad (46)$$

The induction factors a and a' can be found via iterative methods. Starting with an initial guess for a and a' , the iterative method will converge to the final values of these parameters. Once the induction factors are known, the forces on and power from the entire rotor can be calculated as

$$T = \sum_{S_n=1}^n \Delta T_{S_n} \quad (47)$$

where ΔT_{S_n} is calculated using Eq. 24

$$Q = \sum_{S_n=1}^n \Delta Q_{S_n} \quad (48)$$

where ΔQ_{S_n} is calculated using Eq. 38

$$P = Q\omega \quad (49)$$

Finally, the nondimensional thrust, torque and power coefficients for the rotor can be written as

$$C_T = \frac{T}{\frac{1}{2}\rho V_0^2 S_d} \quad (50)$$

$$C_Q = \frac{Q}{\frac{1}{2}\rho V_0^2 R_T S_d} \quad (51)$$

$$C_P = XC_Q = \frac{P}{\frac{1}{2}\rho V_0^3 S_d} \quad (52)$$

III. Results and Discussion

A set of equations to analyze the performance of SUMR rotors capable of segmented multiconing with high coning angles have been derived and implemented in a MATLAB code, BladeMorph. The motivation behind the development of BladeMorph was to combine it with PROPID,^{13,14} an inverse design tool for wind turbine blade design. The SUMR rotor with segmented multiconing will be designed in PROPID which will be subsequently analyzed in BladeMorph, and this process will be streamlined via the use of a graphical user interface developed in MATLAB. However, in this study BladeMorph is being run as a stand-alone computational analysis tool only, and the subsequent results in this section will be presented for an example 13.89 MW SUMR rotor designed in PROPID.

The two-bladed downwind 13.89 MW SUMR rotor designed for this paper is merely an example rotor designed based on the SUMR concept and is not representative of the actual 13 MW SUMR rotor design. Even though the rotor is designed to obtain a rated aerodynamic power of 13.89 MW, the actual power generated by the generator would be about 13.2 MW based on a 95 percent generator efficiency. Consequently, the designed 13.89 MW SUMR rotor will henceforth be called the E-13 SUMR rotor in this paper. The E-13 rotor design was designed to operate at zero cone angle, and the rotor design details have been described in Table 1.

The SUMR rotors, due to their large size, typically operate at high Reynolds number. For instance, the E-13 rotor has a Reynolds number variation along the blade length ranging from nearly 4,000,000 near the hub to about 15,000,000 near the tip. To leverage the best aerodynamic performance from the rotor at such high Reynolds number combined with several structural requirements, a new set of flatback airfoils were designed for the actual 13 MW SUMR rotor. The new set of airfoils were designed in PROFOIL¹⁷⁻¹⁹ and are also used in the design of the E-13 rotor.

As mentioned earlier, PROPID is an inverse design tool for wind turbine blades where the desired aerodynamic properties are prescribed by the designer as the input and the corresponding rotor geometry is obtained as the output. Axial induction factor and lift coefficient distributions were prescribed in PROPID such that the blades operate at optimum values of axial induction factor ($a = \frac{1}{3}$) and the lift coefficients corresponding to the optimum $\frac{C_l}{C_d}$. The chord and twist distributions obtained from PROPID as a result of prescribing the axial induction factor and lift coefficient distributions can be seen in Fig. 8.

The prescribed axial induction factor a and lift coefficient C_l distribution during the design of the E-13 rotor in PROPID has been shown in Fig. 9. The obtained rotor geometry was then analyzed at the design conditions in both BladeMorph and AeroDyn v14 to obtain the prescribed radial distributions. AeroDyn v14^{20,21} is a wind turbine aerodynamic analysis code developed by NREL that interfaces with FAST v8^{22,23} which is NREL's CAE tool for simulation of wind turbine dynamics. FAST v8 is a primary tool used by the ARPA-E SUMR team for analyzing different aspects of wind turbine performance including the aerodynamics, controls, and structures. Figure 9 shows the

Table 1. E-13 Rotor Design Specifications

Design Parameter	Value
Number of Blades	2
Rotor Radius (m)	99.81
Rotor Pitch (deg)	0.45
Design cone angle (deg)	0
Design TSR	9.5
Rated Speed (m/s)	11.3
Average Speed (m/s)	8.5
Rated Power (MW)	13.89

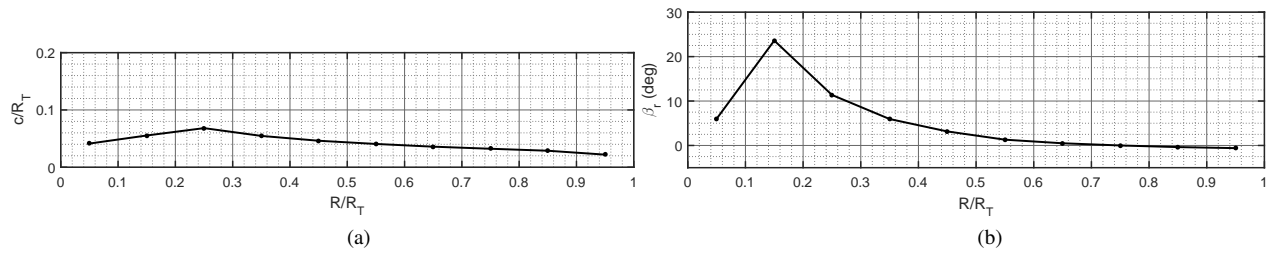


Figure 8. Plots showing geometry for the E-13 rotor blades: a) chord distribution and b) twist distribution.

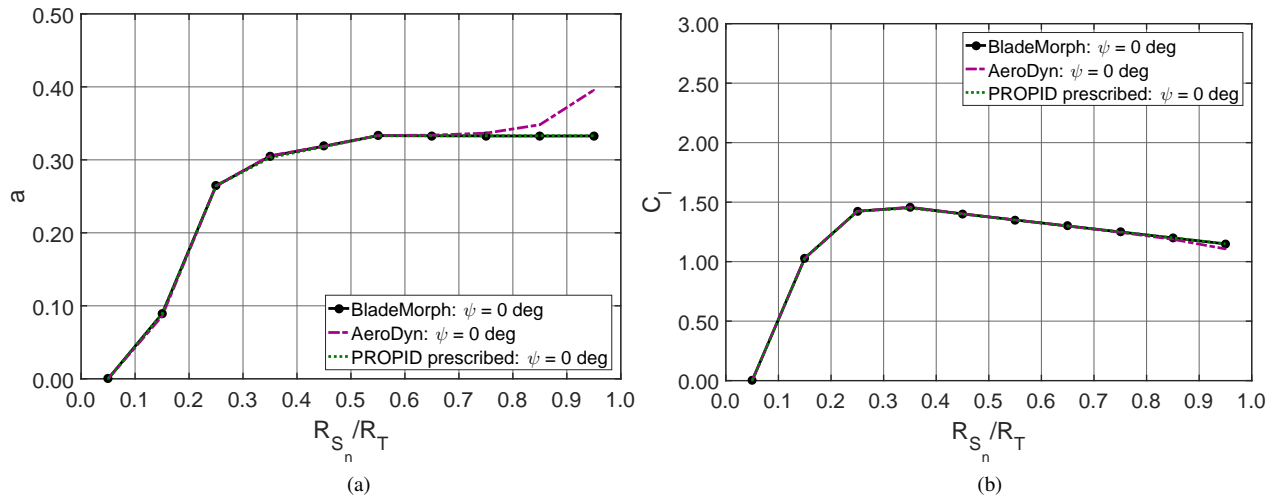


Figure 9. Comparison of radial distribution predictions from BladeMorph and AeroDyn v14 with the prescribed radial distributions for E-13 design in PROPID for: a) axial induction factor a and b) lift coefficient C_l .

radial distribution predictions for the axial induction factor a and lift coefficient C_l from BladeMorph and AeroDyn v14 for the E-13 rotor at the design condition ($V_0 = 8.5$ m/s and $X = 9.5$). On close examination, it can be observed that while BladeMorph was able to predict a and C_l distributions prescribed in PROPID accurately, AeroDyn v14 predictions differed near the tip region.

As explained previously, the SUMR rotors may be morphed to high coning angles for load alignment. Thus, it becomes imperative to analyze the variation in the aerodynamic performance of these rotors when the rotor cone angle is varied. For this purpose, C_P vs X curves were co-plotted at different cone angles, at a fixed tip speed ratio of 9.5. The manner in which morphing the rotor to high cone angles has an effect on the power and thrust coefficients of the E-13 rotor has been shown in Fig. 10. As it can be observed, the C_P and C_T experience a drastic reduction at higher coning angles, with the optimum tip speed ratio values (value of X at which $C_{P_{max}}$ occurs) shifting to lower values at higher coning angles. The reason for the shift of maximum C_P values toward lower X values with increasing coning can be explained by considering the variation in angle of attack distribution along the blade with coning angle, and this will be given later in this section.

As already known, the rotor aerodynamic performance is an integrated effect of the contributions from all the blade elements. Therefore, in order to analyze and describe the rotor performance at different cone angles, variations of pertinent aerodynamic parameters along the blade length with varying coning must be observed. Figure 11 shows the variation in radial distribution with increasing coning for a) angle of attack α , b) angle of attack α upto 10 deg, c) lift coefficient C_l , and d) drag coefficient C_d , e) Reynolds number Re , f) and axial induction factor a distribution, at the fixed average wind speed of 8.5 m/s and design tip speed ratio of 9.5.

An increase in coning angle leads to a reduction in angle of attack as seen from Fig. 11. The reduction in angle of attack with increasing coning at a given tip speed ratio stems from a modification in the flowfield geometry, where only a component of the axial velocity acting normal to the rotor blades is responsible for generation of aerodynamic forces (as seen in Fig. 6). The reduction in angles of attack all along the blade consequently results in a decrease in the C_l and C_d values which subsequently leads to a reduction in the aerodynamic torque and thrust produced. The large

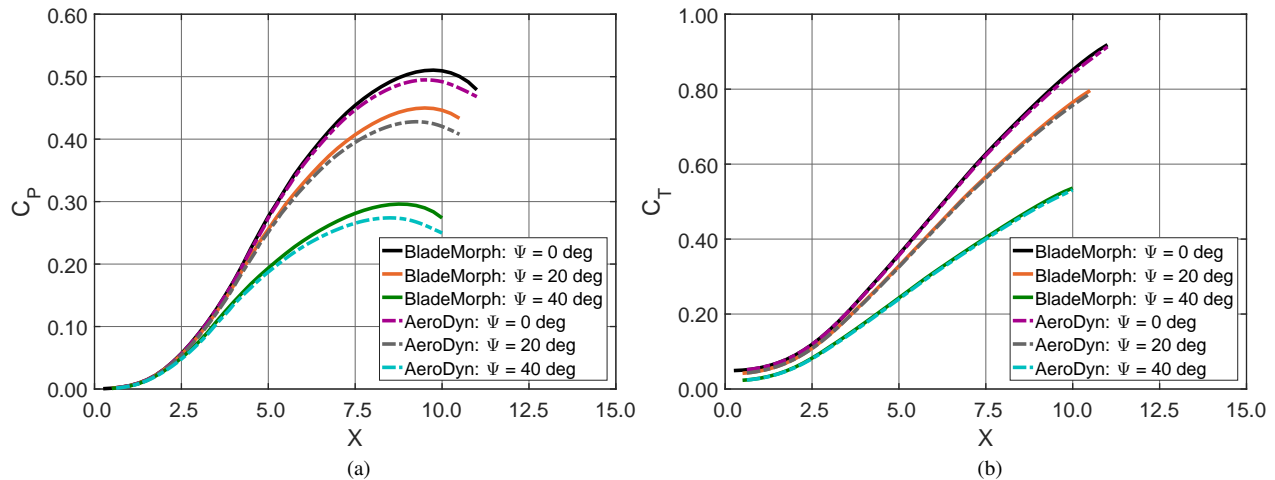


Figure 10. Predictions from BladeMorph and AeroDyn v14 for two different coning angles compared for: a) C_p and b) C_t .

reduction in C_l and C_d values when the rotor coning angle is increased from 0 to 40 deg is what causes the significant reduction in C_p and C_t values seen in Fig. 10.

As observed earlier in Fig. 10, the maximum C_p at higher coning is achieved at lower values of tip speed ratio. Lower values of X at a given wind speed V_0 imply lower values of the tangential velocity V_T which results in higher angles of attack along the blade (see Fig. 7). As discussed previously, when coned at a higher angles, the angles of attack experience a reduction along the blade length. It is also known that the $C_{P_{max}}$ for a given coning angle is achieved when the blades operate at the optimum L/D distribution. Keeping the aforementioned facts in mind, it becomes apparent that the lowering of angles of attack with an increasing coning angle from the optimum values corresponding to the best L/D at zero coning is compensated by an increase in the angles of attack due to operating at a lower tip speed ratio. In other words, at higher coning only a component of the axial velocity is responsible for generation of aerodynamic forces; however, a lower tangential velocity due to operating at a lower tip speed ratio helps increase the angles of attack back to the optimum value which results in a maximum value of C_p at a lower tip speed ratio for higher cone angles.

Figure 11 also shows a marginal variation in Reynolds number distribution with increasing coning angle. However, these variations are not as significant as the variations in other aerodynamic parameters. Since the Reynolds number was defined based on the local chord length of the blade and because the local chord length is unchanged with coning angle, it can be concluded that the changes in the net relative velocity W at a given wind speed and tip speed ratio with higher coning is negligible. The reason for the small change in W can be obtained by looking at Eq. 17. For a given wind speed V_0 and tip speed ratio X , changing the coning angle affects only V_a while V_T value is not much affected. Even though the tangential induction factor a' term in V_T varies with coning, its value is typically small compared with the other terms. Since the tip speed V_T values are larger than the axial velocity values V_a , the value of the net relative velocity W remains largely unaffected, especially toward the outboard region where the tip speeds are much larger than the axial velocities. The small variation in the net relative velocity along the blade with higher coning also implies that the dynamic pressure does not change much along the blade with higher coning.

It is also interesting to note that with increasing coning angle, the axial induction factor increases toward the outboard region when compared with zero coning, while it reduces toward the hub. Such a variation in the axial induction distribution with coning angle implies that the E-13 rotor decelerates the flow toward the tip more at higher coning angles compared with the zero coning case, while the opposite is true for the inboard sections where the E-13 rotor decelerates the flow less toward the hub at higher coning angles compared with the zero deg coning case.

Observing Fig. 10 again, it can be seen that AeroDyn v14 is underpredicting C_p values when compared with BladeMorph. AeroDyn v14 is also underpredicting C_t values; however, the differences between predictions from BladeMorph and AeroDyn v14 are small for C_t . The reason for the slight differences between predictions from AeroDyn v14 and BladeMorph can be obtained by looking at the radial distribution comparisons shown in Fig. 11. On inspecting the axial induction factor distribution in Fig. 11a, a slight difference between AeroDyn v14 and BladeMorph predictions can be seen toward the tip. Similar differences can also be seen in the angle of attack and C_l

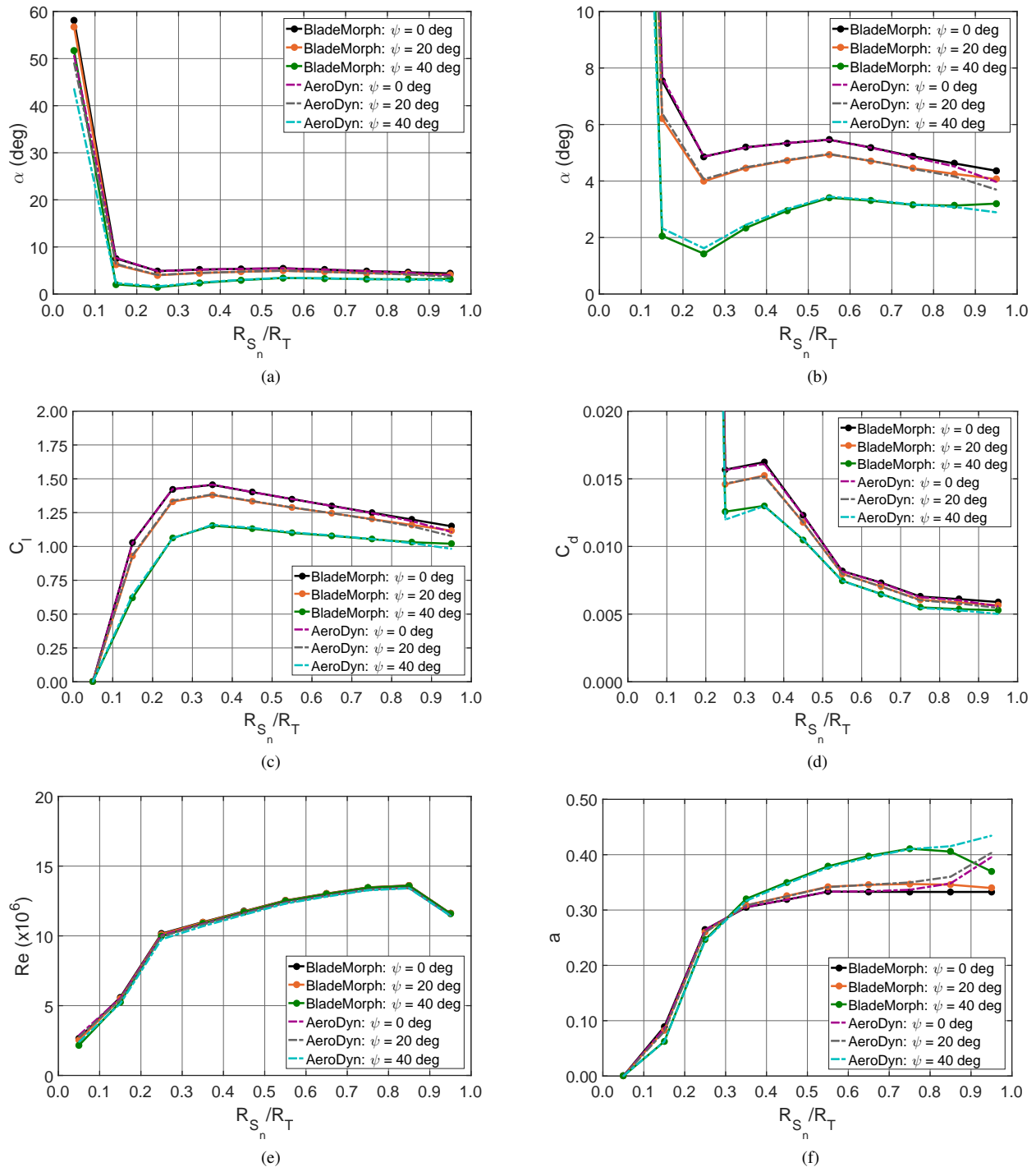


Figure 11. Variation in radial distribution predictions for: a) angle of attack α , b) angle of attack α up to 10 deg, c) lift coefficient C_l , d) drag coefficient C_d , e) Reynolds number Re , and f) axial induction factor a , obtained from BladeMorph and AeroDyn v14 for three different coning angles.

distribution curve comparisons. Upon careful observation, it can be seen that even though BladeMorph and AeroDyn v14 predictions are in good agreement for nearly 75 percent of the blade, the differences in predictions near the tip region caused noticeable differences in the $C_{P_{max}}$ predictions from both codes. Such a trend displays the importance of obtaining the correct aerodynamic characteristics near the outboard section of the blades, and the importance of

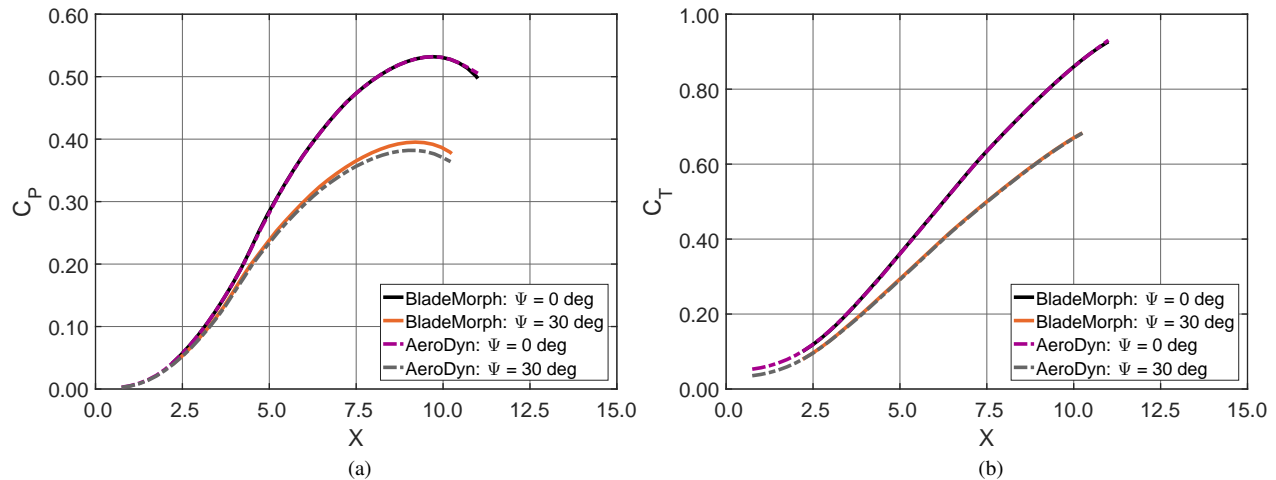


Figure 12. Predictions from BladeMorph and AeroDyn v14 without the tip and hub loss models for two different coning angles compared for: a) C_p and b) C_T .

using accurate tip loss models. The differences in predictions near the tip region was speculated to be a result of differences in the tip loss model implementation and hence, both the tip loss and hub loss models were turned off in AeroDyn v14 and BladeMorph for the purpose of comparison. Figure 12 shows the C_p and C_T curve comparisons for 0 and 30 deg coning cases.

Upon inspection of Fig. 12, it becomes apparent that the differences between C_p and C_T predictions in Fig. 10 were indeed caused by the difference between tip loss model implementations in the two codes. It is worth noting that despite better agreement at higher coning between AeroDyn v14 and BladeMorph when the tip and hub loss models were turned off, AeroDyn v14 still underpredicts C_p at higher coning, when compared with BladeMorph.

IV. Conclusions

An aerodynamic analysis tool was developed by modifying the BEM model proposed by Hibbs and Radkey¹¹ to extend the analysis capability of the code to segmented rotors with multiple coning angles. The new model can be used to analyze SUMR rotors in various morphing configurations with high coning angles depending on the wind speed. The model allows for the blade to be discretized in a nonuniform fashion based on the its hinge locations. The model was implemented in a MATLAB code, BladeMorph which will be combined with PROPID via a graphical user interface to facilitate design and analysis of the SUMR rotors. Additional capabilities include aerodynamic analysis of SUMR rotor with a morphing and pitch schedule, where the cone angle and the blade pitch can vary with wind speed.

An example 2-bladed downwind 13.89 MW rotor based on the SUMR concept, called the E-13 rotor in this paper, was designed in PROPID and analyzed in BladeMorph and AeroDyn v14. In general, BladeMorph and AeroDyn v14 predictions at different coning angles were found to be in good agreement, with AeroDyn v14 underpredicting $C_{P_{max}}$ when compared with BladeMorph. To better understand the slight differences in $C_{P_{max}}$ values at different coning angles, radial distribution data from BladeMorph and AeroDyn v14 were co-plotted for varying coning angles. It was found that both BladeMorph and AeroDyn v14 predictions were in good agreement for nearly 75 percent of the blade, with slight differences in the predictions occurring near the tip region. The tip loss models were consequently turned off in both codes for the purpose of comparison, and extremely good agreement in C_p curve predictions from both codes was found for zero coning. On turning off the tip loss models in both codes, agreement at higher coning also improved. However, AeroDyn v14 still underpredicted $C_{P_{max}}$ at higher coning when compared with BladeMorph.

V. Future Work

As a part of the SUMR project, there are currently on-going efforts to develop wind tunnel testing capability in the University of Illinois at Urbana-Champaign for subscale testing of highly coned rotors.²⁴ One of the main purposes of these tests is to validate BladeMorph and other BEMT based computational codes for highly coned rotors such

as AeroDyn v14. Due to practical limitations, a perfect scaling of the extreme-scale SUMR rotors is not possible for testing in the UIUC wind tunnel. However, since these tests are being conducted to validate BladeMorph and other computational codes, an entirely new rotor will be designed to be tested at low Reynolds number in the UIUC open-return 2.8 x 4 ft subsonic wind tunnel.²⁴ Following validation, BladeMorph will be subsequently integrated with PROPID via a graphical user interface designed in MATLAB for the purpose of rapid aerodynamic design and analysis of extreme-scale SUMR rotors with possible segmented multiconging.

VI. Acknowledgment

The information, data, or work presented herein was funded in part by the Advanced Research Projects Agency-Energy (ARPA-E), U.S. Department of Energy, under Award Number DE-AR0000667. The views and opinions of authors expressed herein do not necessarily state or reflect those of the United States Government or any agency thereof.

References

- ¹U.S. Department of Energy, "Wind Vision: A New Era of Wind Power in the United States," <http://energy.gov/eere/wind/wind-vision>, 2017–.
- ²Advanced Research Projects Agency-Energy (ARPA-E), "50 MW Segmented Ultralight Morphing Rotors for Wind Energy," <https://arpa-e.energy.gov/?q=slick-sheet-project/ultra-large-wind-turbine>, 2015–.
- ³Steele, A., Icher, B., Qin, C., Loth, E., Selig, M. S., and Moriarty, P. J., "Aerodynamics of an Ultralight Load-Aligned Rotor for Extreme-Scale Wind Turbines," AIAA Paper 2013-0914, Grapevine, Texas, 2013.
- ⁴Sandia National Laboratories, "Enormous blades could lead to more offshore energy in U.S.," https://share.sandia.gov/news/resources/news_releases/big_blades/#.WBc2qugrJaS, 2016–.
- ⁵ARPA-E SUMR Project, "Segmented Ultralight Morphing Rotor," <https://sumrwind.com/>, 2017–.
- ⁶Icher, B., Steele, A., Loth, E., Moriarty, P. J., and Selig, M. S., "A Morphing Downwind-Aligned Rotor Concept Based on a 13-MW Wind Turbine," *Wind Energy*, Vol. 19, No. 4, 2016, pp. 625–637.
- ⁷Mikkelsen, R., Sørensen, J. N., and Shen, W. Z., "Modelling and Analysis of the Flow Field Around a Coned Rotor," *Wind Energy*, Vol. 4, No. 3, 2001, pp. 121–135.
- ⁸Madsen, H. A., Bak, C., Døssing, M., Mikkelsen, R., and Øye, S., "Validation and Modification of the Blade Element Momentum Theory Based on Comparisons with Actuator Disc Simulations," *Wind Energy*, Vol. 13, No. 4, 2010, pp. 373–389.
- ⁹Crawford, C., "Re-examining the Precepts of the Blade Element Momentum Theory for Coning Rotors," *Wind Energy*, Vol. 9, No. 5, 2006, pp. 457–478.
- ¹⁰Crawford, C. and Platts, J., "Updating and Optimization of a Coning Rotor Concept," *Journal of Solar Energy Engineering*, Vol. 130, No. 3, 2008, pp. 031002–1–031002–8.
- ¹¹Hibbs, B. and Radkey, R., "Small Wind Energy Conversion Systems (SWECS) Rotor Performance Model Comparison Study," Tech. Rep. RFP-4074/13470/36331/81-0, Aerovironment, Inc., 145 Vista Avenue, Pasadena, California, Nov 1981.
- ¹²Hibbs, B. and Radkey, R., "Calculating Rotor Performance with the Revised PROP Computer Code," *Horizontal-Axis Wind System Rotor Performance Model Comparison—A Compendium*, Wind Energy Research Center, Rockwell International, Rocky Flats Plant, Golden, CO, RFP-3508, UC-60, 1983.
- ¹³Giguere, P. and Selig, M. S., "Aerodynamic Blade Design Methods for Horizontal Axis Wind turbines," 13th Annual Canadian Wind Energy Association Conference and Exhibition, Quebec, Canada, October 19–22, 1997.
- ¹⁴Selig, M. S. and Tangler, J. L., "Development and Application of a Multipoint Inverse Design Method for Horizontal Axis Wind turbines," *Wind Engineering*, Vol. 19, No. 2, 1995, pp. 91–105.
- ¹⁵Eggleston, D. M. and Stoddard, F. S., *Wind Turbine Engineering Design*, Van Nostrand Reinhold Company, 1987.
- ¹⁶Crawford, C., "Re-Examining The Precepts of the Blade Element Momentum Theory for Coning Rotors," *Wind Energy*, Vol. 9, No. 5, 2006, pp. 457–478.
- ¹⁷Selig, M. S. and Maughmer, M. D., "A Multipoint Inverse Airfoil Design Method Based on Conformal Mapping," *AIAA Journal*, Vol. 30, No. 5, 1992, pp. 1162 – 1170.
- ¹⁸Selig, M. S. and Maughmer, M. D., "Generalized Multipoint Inverse Airfoil Design," *AIAA Journal*, Vol. 30, No. 11, 1992, pp. 2618 – 2625.
- ¹⁹Selig, M. S., "Multipoint Inverse Design of Isolated Airfoils and Airfoils in Cascade in Incompressible Flow," Ph.D. Dissertation, Dept. of Aerospace Engineering, Pennsylvania State Univ., University Park, PA, May 1992.
- ²⁰Moriarty, P. J. and Hansen, A. C., "AeroDyn Theory Manual," Tech. Rep. NREL/EL-500-36881, National Renewable Energy Laboratory, 1617 Cole Boulevard, Golden, Colorado, Dec 2005.
- ²¹Jonkman, J., Damiani, R., and Jonkman, B., NWTC Information Portal, "AeroDyn v14," <https://nwtc.nrel.gov/AeroDyn14>, 2016–.
- ²²Jonkman, J. and Jonkman, B., NWTC Information Portal, "FAST v8," <https://nwtc.nrel.gov/FAST8>, 2016–.
- ²³Jonkman, J. M. and Buhl Jr., M., "FAST User's Guide," Tech. Rep. NREL/EL-500-38230, National Renewable Energy Laboratory, 1617 Cole Boulevard, Golden, Colorado, Aug 2005.
- ²⁴Ananda, G. K., Bansal, S., and Selig, M., "Subscale Testing of Horizontal-Axis Wind Turbines," AIAA Paper 2017-4216, 35th AIAA Applied Aerodynamics Conference, Denver, CO, June 2017.